

Radial fingering under arbitrary viscosity and density ratios

Pedro H. A. Anjos, Eduardo O. Dias,^{*} and José A. Miranda[†]

Departamento de Física, Universidade Federal de Pernambuco, Recife, Pernambuco 50670-901, Brazil

(Received 25 April 2017; published 21 August 2017)

We study viscous fingering formation in radial Hele-Shaw cell geometry considering the combined action of capillary and inertial effects for arbitrary values of viscosity and density ratios. We tackle the problem by employing a perturbative mode-coupling approach and focus our attention on weakly nonlinear stages of the dynamics. If inertial effects are neglected, our theoretical results indicate that the shape of the resulting interfacial patterns is significantly affected by changes in the viscosity ratio. Under such conditions, the growing fingers tend to proliferate through a repeated ramification process (e.g., by finger bifurcation, quadrifurcation, etc.) as the capillary number is increased. Nevertheless, we find that this scenario is dramatically altered when inertia is taken into account. When inertia is relevant, the conventional finger splitting morphologies are replaced by three-lobed structures, characterized by the occurrence of sidebranching phenomena. We verify that slightly different types of sidebranched patterns arise, presenting either wide or sharp fingertips, for a range of capillary numbers and density ratios.

DOI: [10.1103/PhysRevFluids.2.084004](https://doi.org/10.1103/PhysRevFluids.2.084004)

I. INTRODUCTION

One of the most influential examples of pattern formation in fluid systems is the viscous fingering (or Saffman-Taylor) instability [1]. This acclaimed interfacial instability arises when a fluid displaces another of higher viscosity in the confined geometry of a Hele-Shaw cell. Such a cell is a device composed of two narrowly spaced parallel glass plates where an effectively two-dimensional (2D) flow takes place. Over the past several decades the viscous fingering phenomenon has been extensively studied and has become a prototypical problem in fluid dynamics, of significant scientific and technological relevance [2]. A popular and widely investigated version of the Saffman-Taylor problem is the radial (or circular) flow case driven by injection [3–5]. It involves the radial invasion of the less viscous fluid that is injected into the more viscous one through a small hole located at the center of the upper glass plate. Numerous careful experiments [5–11] and sophisticated numerical simulations [12–14] reveal that under radial flow, as the fluid-fluid interface grows, fingerlike structures form, spread outward, and split at their tips, originating multiply ramified interfacial patterns.

Despite the large number of numerical and experimental studies already performed, most work on the development of radial fluid fingering in the literature has focused on the case in which the displaced fluid (of viscosity η_2) is much more viscous than the displacing fluid (of viscosity η_1). So existing studies concentrate on situations involving a very large or even an infinite viscosity ratio $\beta = \eta_2/\eta_1$. This is in part due to the fact that these are precisely the situations of interest for some important practical applications such as gas-oil injection in enhanced oil recovery processes [15,16]. Another practical reason is related to the fact that a gas is often dewetting and the liquid (e.g., oil) used is usually wetting, making this a very clean system to study experimentally. On the academic side, large- and infinite- β limits are often considered due to their greater simplicity in describing the system theoretically. Therefore, the study of radial Hele-Shaw cell displacements and related pattern-formation issues for an arbitrary viscosity ratio β , where the viscosities of both fluids are considered non-negligible, has not received much attention.

^{*}eduardodias@df.ufpe.br

[†]jme@df.ufpe.br

Actually, only a few groups have performed a systematic evaluation of pattern-forming elements of the radial viscous fingering problem under arbitrary viscosity ratio conditions. This has been done experimentally in Refs. [17,18] and numerically in Ref. [19]. The experimental investigations carried out in [17,18] explored the advance-time regime in which complex, fully nonlinear structures are formed. Under such conditions, it has been shown that a large variability of interfacial morphologies is found where distinctively different patterns are created as the viscosity ratio β is varied. Consistently with previous experimental results [5–11], the traditional large-viscosity-ratio patterns observed in Refs. [17,18] present long fingers growing from a small circular region in which the outer fluid is completely displaced. Nevertheless, as the viscosity ratio is decreased, considerably dissimilar fingering shapes arise where the mentioned inner circular region increases dramatically while the lengths of the growing fingers tend to decrease. For very illustrative examples of such viscosity-ratio-dependent pattern-forming behaviors, we refer the reader to Fig. 2 in Ref. [17] and Fig. 1 in Ref. [18]. These experimental findings do show that the morphology of the fluid-fluid interface in radial Hele-Shaw flows is strongly influenced by the viscosity ratio β .

The long-time morphological features experimentally detected in Refs. [17,18] for varying viscosity ratios have been probed recently by Jackson *et al.* [19], who utilized numerical techniques. In Ref. [19] the authors developed an effective boundary integral method and used intensive numerical simulations to examine the impact of the viscosity ratio on radial viscous fingering across a range of capillary numbers Ca (the relative measure between viscous and surface tension forces). In agreement with Refs. [17,18], their advance-time numerical results revealed that the fingering characteristics obtained for lower viscosity ratios are quite different from those commonly observed under large- or infinite-viscosity-ratio circumstances [5–14]. In addition to the interface features already identified experimentally in Refs. [17,18], the simulations presented in Ref. [19] have also highlighted other interesting dynamic aspects of the evolving patterns as the viscosity ratio β is changed. First, they have verified that the near stagnation points (i.e., points at which the interface velocity tends to zero) located on the bases of the fingers (the so-called fjords [10,11]) found in large- and infinite-viscosity-ratio flows are not encountered under low-viscosity-ratio conditions. In the low- β case, the finger bases move away from their starting positions. Moreover, their fully nonlinear simulations indicate that the number of fingers at the first interface ramification increases with the capillary number, leading to interfacial fronts presenting different profiles as Ca is modified. It has also been found that the finger base motion was independent of the capillary number. The important fully nonlinear results obtained in Ref. [19] demonstrated that the various regimes of radial Hele-Shaw flows can be properly and conveniently described by just two controlling parameters: β and Ca .

In spite of the efforts dedicated in Refs. [17–19] to improve the understanding of the advance time, completely nonlinear dynamics of viscous fingering patterns in radial Hele-Shaw flows under arbitrary viscosity-ratio and capillary number conditions, an analytical study of the evolution of the system is still missing. Due to the highly nonlinear and nonlocal nature of the long-time interfacial dynamics examined in Refs. [17–19], analytical comprehension is notably scarce. As a consequence, a predominantly analytical assessment of the influence of β and Ca on pattern-formation mechanisms during early nonlinear stages of radial Hele-Shaw flows remains elusive.

In this work, our first goal is to offer a suitable analytical description for the development of viscous fingering patterns in radial Hele-Shaw cells for arbitrary viscosity ratio β for a range of capillary numbers Ca . In contrast to what has been previously done in Refs. [17–19], we focus on the weakly nonlinear time regime and address the onset of nonlinearities. By doing this, we can capture the key dynamical behaviors at the earliest nonlinear level and provide useful insight into the most prominent pattern-forming responses identified in Refs. [17–19]. More specifically, we use a weakly nonlinear mode-coupling approach to try to detect key nonlinear aspects such as the variability of interface profiles and related finger proliferation as Ca is varied and the suppression of finger base stagnation effects for lower β , already in the early nonlinear regime.

Additionally, we go beyond the physics exploited in Refs. [17–19] and investigate how inertia affects the radial Hele-Shaw fingering dynamics for the general case in which both the displacing and the displaced fluids have non-negligible viscosities and densities. The inclusion of inertia in

the present problem was motivated by the increased attention that such an important physical effect has been receiving in the study of the Saffman-Taylor instability [20–29]. These innovative viscous fingering studies have unveiled a wealth of inertially induced pattern shapes and the emergence of still unexplored dynamical responses. Here we show that when inertial effects are taken into account, in addition to the viscosity ratio β and capillary number Ca , one needs to consider the role played by the density ratio $\alpha = \rho_2/\rho_1$ as well as the influence of the Reynolds number Re , a physical parameter that quantifies the effect of inertia on the system. By considering the combined action of β , Ca , α , and Re we revisit the fundamental fluid dynamics pattern-forming problem studied in Refs. [17–19] and investigate how the weakly nonlinear aspects of the dynamics are modified through the consideration of inertial effects.

The outline of the rest of the paper is as follows. Section II lays out the derivation of the weakly nonlinear equations for Hele-Shaw flows in radial geometry when inertial effects are taken into account for arbitrary values of viscosity and density ratios and for various magnitudes of the capillary number. Our mode-coupling theory has a generalized gap-averaged nonlinear Darcy law equation as a starting point and employs a second-order perturbative approach that permits access to the onset of intrinsically nonlinear pattern-forming mechanisms. In Sec. III we analyze various facets of the viscous fingering pattern-formation dynamics in the weakly nonlinear regime both in the absence (Sec. III A) and in the presence (Sec. III B) of inertial effects. While doing this, we explore the influence of the controlling parameters of the system (β , Ca , α , and Re) on the development of the nonlinear interfacial structures. Our main results and conclusions are briefly summarized in Sec. IV.

II. GOVERNING EQUATIONS

The physical system we study is very simple: It is composed of two Newtonian immiscible fluids located in the spatially constrained environment of a Hele-Shaw cell (see Fig. 1). The Hele-Shaw apparatus consists of two narrowly spaced, parallel glass plates separated by a gap space of width b . Consider that the inner fluid has viscosity η_1 and density ρ_1 , while the outer fluid has viscosity η_2 and density ρ_2 . At the interfacial boundary where the two fluids meet there exists a surface tension σ . We study viscous flow in a radial Hele-Shaw cell setup, where the less viscous inner fluid is injected radially at the center of the cell at a constant injection rate Q (equal to the area covered per unit time), displacing the more viscous outer fluid.

Initially, at $t = 0$, we have a circular fluid-fluid interface of radius $R(t = 0) = R_0$. As the flow takes place, the less viscous fluid pushes away the more viscous one, leading to the formation of Saffman-Taylor fingering deformations. In the context of our perturbative scheme, the deformed two-fluid interface is described as $\mathcal{R}(\theta, t) = R(t) + \zeta(\theta, t)$, where $R = R(t) = \sqrt{R_0^2 + Qt/\pi}$ is the time-dependent unperturbed radius and θ represents the azimuthal angle. The net interface perturbation is represented by $\zeta(\theta, t) = \sum_{n=-\infty}^{+\infty} \zeta_n(t) \exp(in\theta)$. Here $\zeta_n(t)$ are the Fourier amplitudes with integer wave numbers n . We follow Ref. [30] such that our weakly nonlinear perturbative approach keeps terms up to the second order in ζ . Note that in the Fourier expansion of ζ , we include the $n = 0$ mode to maintain the area of the perturbed shape independent of the perturbation

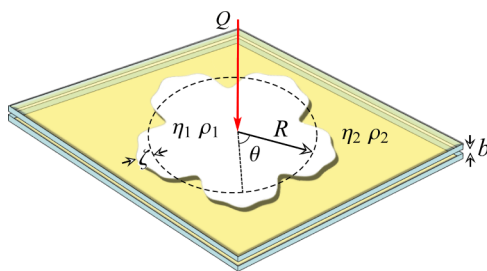


FIG. 1. Representative sketch of the injection-driven fluid motion in a radial Hele-Shaw cell geometry.

ζ . Then mass conservation imposes that the zeroth mode is written in terms of the other modes as $\zeta_0 = -(1/2R) \sum_{n \neq 0} |\zeta_n(t)|^2$. In this section we aim to derive an equation of motion describing the time evolution of the perturbation amplitudes $\zeta_n(t)$ in the weakly nonlinear regime.

With the inclusion of inertial effects, the governing hydrodynamic equations of the system are represented by a gap-averaged nonlinear generalized Darcy law equation [20–25]

$$\rho_j \left[\frac{\partial \mathbf{u}_j}{\partial t} + \frac{6}{5} (\mathbf{u}_j \cdot \nabla) \mathbf{u}_j \right] = -\nabla p_j - \frac{12\eta_j}{b^2} \mathbf{u}_j \quad (1)$$

and by a 2D continuity equation for an incompressible fluid

$$\nabla \cdot \mathbf{u}_j = 0. \quad (2)$$

In these two equations, $\mathbf{u}_j = \mathbf{u}_j(r, \theta)$ and $p_j = p_j(r, \theta)$ are the velocity and the pressure for fluids $j = 1, 2$, respectively. It should be noted that the coefficients appearing in front of the terms $\partial \mathbf{u}_j / \partial t$ and $(\mathbf{u}_j \cdot \nabla) \mathbf{u}_j$ may vary depending on the way the gap averaging is performed, but are always of order 1.

To get the equation of motion for the fluid-fluid interface, we rewrite Eq. (1) for each of the fluids in terms of the velocity potential ϕ_j [23,24], where $\mathbf{u}_j = -\nabla \phi_j$, and then subtract the resulting equations from each other, evaluated at the perturbed interface $r = \mathcal{R}$. The result is a *dimensionless* equation of motion

$$\text{Re} \left\{ \frac{1}{\alpha} \left[\frac{\partial \phi_1}{\partial t} - \frac{3}{5} |\nabla \phi_1|^2 \right] - \left[\frac{\partial \phi_2}{\partial t} - \frac{3}{5} |\nabla \phi_2|^2 \right] \right\}_{r=\mathcal{R}} = \left[p_1 - p_2 - \frac{\phi_1}{\beta} + \phi_2 \right]_{r=\mathcal{R}}, \quad (3)$$

where the parameters $\alpha = \rho_2 / \rho_1$ and $\beta = \eta_2 / \eta_1$ are the density and the viscosity ratios mentioned in Sec. 1. In Eq. (3) lengths are rescaled by $L = R_0$ and velocities by a characteristic velocity $U = Q / R_0$. The Reynolds number quantifies the effect of inertia on the system and is defined as

$$\text{Re} = \frac{\rho_2 U b^2}{12 \eta_2 L}. \quad (4)$$

For typical experimental parameters [1–11] the Reynolds number is very small ($10^{-3} \leq \text{Re} \leq 10^{-2}$) and can be safely disregarded. However, for situations involving larger gap widths, higher interfacial velocities, and displaced fluids of lower viscosities, as in the cases studied in Refs. [20,23], the Reynolds number can be considerably larger ($\text{Re} = 10^{-1}$) and inertial effects must be taken into account. Note that, from this point onward, we work with the dimensionless version of the equations.

It should be emphasized that the great majority of works on viscous fingering in Hele-Shaw cells (see, for instance, [1,2,5–19] and references therein) simply neglect the effect of inertia. This is justified by the fact that, under traditional Hele-Shaw conditions (i.e., low flow velocities, small gap width, highly viscous displaced fluid, etc.), one has a nearly-zero-Reynolds-number situation in a way that the action of inertia can be safely disregarded. However, if the conditions are such that the flow velocity is considerably high, the cell gap thickness is not so small, or if the displaced fluid is not excessively viscous, one can have a sizable-Reynolds-number flow where inertial effects must be taken into account [20–29]. Within a non-negligible Reynolds number scenario, the usual Darcy law approach of the viscous fingering problem [2] must be replaced by the more general description involving Eq. (1). In particular, if one wishes to study the evolution of the fluid-fluid interface in a situation that includes inertia and considers arbitrary values of β and α , Eq. (3) should be used. Notice that the conventional equation of motion valid for the noninertial situation can be readily recovered from Eq. (3) by considering the limiting case in which $\text{Re} = 0$. Note that in this limit, the influence of the density ratio α drops out automatically.

In order to study the motion of the deformed two-fluid interface, we need to relate the velocity potential (which obeys Laplace's equation $\nabla^2 \phi_j = 0$) with the position of the interface $\mathcal{R}(\theta, t)$. This

can be done by using the kinematic boundary condition

$$\frac{\partial \mathcal{R}}{\partial t} = \left[\frac{1}{r^2} \frac{\partial r}{\partial \theta} \frac{\partial \phi_j}{\partial \theta} - \frac{\partial \phi_j}{\partial r} \right]_{r=\mathcal{R}}, \quad (5)$$

which states that the normal components of each fluid velocity are continuous at the interface. In addition, to fully specify the fluid dynamics problem, we need one more equation related to the pressure jump across the interface. The pressure boundary condition is expressed by the Young-Laplace equation [2]

$$(p_1 - p_2)|_{r=\mathcal{R}} = \frac{1}{\text{Ca}} \kappa \Big|_{r=\mathcal{R}}, \quad (6)$$

where the in-plane interfacial curvature is denoted by κ and

$$\text{Ca} = \frac{12\eta_2 Q R_0}{\sigma b^2} \quad (7)$$

represents the capillary number that provides a relative measure of viscous to surface tension forces.

Considering the incompressibility condition (2), we define Fourier expansions for the velocity potential. Then we write ϕ_j in terms of the perturbation amplitudes ζ_n by considering the condition (5). Substituting these relations and the pressure jump condition (6) into Eq. (3), always keeping terms up to second order in ζ , and Fourier transforming, we finally find the equation of motion for the perturbation amplitudes (for $n \neq 0$)

$$\begin{aligned} \text{Re} \ddot{\zeta}_n + \frac{1}{2\pi} \left\{ \frac{\alpha}{\beta} \left(\frac{\beta+1}{\alpha+1} \right) - \text{Re} \frac{1}{R^2} \left[\left(\frac{\alpha-1}{\alpha+1} \right) \frac{|n|}{5} - 2 \right] \right\} \dot{\zeta}_n \\ - \left\{ \Lambda(n) - \text{Re} \frac{1}{4\pi^2 R^4} \left[\left(\frac{\alpha-1}{\alpha+1} \right) |n| - 1 \right] \right\} \zeta_n \\ = + \frac{1}{4\pi^2} \sum_{n' \neq 0} [\mathcal{F}(n, n') + \text{Re} \mathcal{H}(n, n')] \zeta_{n'} \zeta_{n-n'} + \frac{1}{2\pi} \sum_{n' \neq 0} [\mathcal{K}(n, n') + \text{Re} \mathcal{I}(n, n')] \dot{\zeta}_{n'} \zeta_{n-n'} \\ + \text{Re} \sum_{n' \neq 0} [\mathcal{G}(n, n') \ddot{\zeta}_{n'} \zeta_{n-n'} + \mathcal{J}(n, n') \dot{\zeta}_{n'} \dot{\zeta}_{n-n'}], \end{aligned} \quad (8)$$

where the overdot denotes total time derivative and

$$\Lambda(n) = \left(\frac{\alpha}{1+\alpha} \right) \left\{ \frac{1}{4\pi^2 R^2} \left[\left(\frac{\beta-1}{\beta} \right) |n| - \left(\frac{\beta+1}{\beta} \right) \right] - \frac{|n|(n^2-1)}{2\pi \text{Ca} R^3} \right\}. \quad (9)$$

The mode-coupling terms are given by

$$\mathcal{F}(n, n') = \left(\frac{\alpha}{\alpha+1} \right) \frac{|n|}{R} \left\{ \left(\frac{\beta-1}{\beta} \right) \frac{1}{R^2} \left[\frac{1}{2} - \text{sgn}(nn') \right] - \frac{2\pi}{\text{Ca} R^3} \left[1 - \frac{n'}{2}(3n'+n) \right] \right\}, \quad (10)$$

$$\mathcal{K}(n, n') = \left(\frac{\alpha}{\alpha+1} \right) \frac{1}{R} \left\{ \left(\frac{\beta-1}{\beta} \right) |n| [1 - \text{sgn}(nn')] - \left(\frac{\beta+1}{\beta} \right) \right\}, \quad (11)$$

$$\mathcal{G}(n, n') = \frac{1}{R} \left\{ \left(\frac{\alpha-1}{\alpha+1} \right) |n| [1 - \text{sgn}(nn')] - 1 \right\}, \quad (12)$$

$$\mathcal{H}(n, n') = \frac{|n|}{R^5} \left\{ \left[\frac{|n|}{5} + 2 \left(\frac{\alpha-1}{\alpha+1} \right) \right] \text{sgn}(nn') - \left(\frac{\alpha-1}{\alpha+1} \right) - \frac{|n'|}{5} - \frac{3}{5} \left(\frac{\alpha-1}{\alpha+1} \right) \text{sgn}[n'(n-n')] \right\}, \quad (13)$$

$$\mathcal{I}(n, n') = \frac{|n|}{R^3} \left\{ \left[\frac{|n|}{5} - \left(\frac{\alpha - 1}{\alpha + 1} \right) \right] \text{sgn}(nn') + \left(\frac{\alpha - 1}{\alpha + 1} \right) - \frac{|n'|}{5} - \frac{6}{5} \left(\frac{\alpha - 1}{\alpha + 1} \right) \text{sgn}[n'(n - n')] - \left(\frac{\alpha - 1}{\alpha + 1} \right) \text{sgn}[n(n - n')] \right\}, \quad (14)$$

and

$$\mathcal{J}(n, n') = \frac{1}{R} \left\{ \frac{3}{5} |n| \left(\frac{\alpha - 1}{\alpha + 1} \right) \{1 - \text{sgn}[n'(n - n')]\} - |n| \left(\frac{\alpha - 1}{\alpha + 1} \right) \text{sgn}(nn') - 1 \right\}, \quad (15)$$

where the sgn function equals ± 1 according to the sign of its argument.

Expressions (8)–(15) represent the mode-coupling equations of a quite general viscous fingering situation in a radial Hele-Shaw cell that considers the action of inertial and capillary effects, which are valid for arbitrary values of the viscosity and density ratios. Observe that the system is handily described by four controlling physical parameters: Re , Ca , β , and α . Note that when $\text{Re} = 0$ and $\alpha \gg 1$ Eq. (8) reproduces the simpler results obtained in Ref. [30] for the corresponding problem without considering inertia. In this case, $2\pi[\beta/(\beta + 1)]\Lambda(n)$ is the linear growth rate of the noninertial system. Likewise, when $\text{Re} \neq 0$, $\beta \gg 1$, and $\alpha \gg 1$ Eq. (8) recovers the more straightforward one-fluid version of the problem with inertia, studied in Ref. [25].

Equation (8) is a considerably intricate second-order ordinary differential equation presenting time-dependent coefficients [in view of the fact that $R = R(t)$]. The complexity of such a nonlinear equation should not be underestimated, in the sense that it is not really amenable to a purely analytical treatment. Even the mode-coupling expressions written for a few interacting Fourier modes [obtained from Eqs. (8)–(15)] are usually too long and cluttered to be managed analytically. Despite this theoretical impediment, as will become clear during the course of this paper, our mode-coupling approach still offers the possibility to gain physical insight into important morphological aspects of the arising radial Hele-Shaw flow patterns. This is true in spite of the significantly general circumstances we consider in this work, in which the physical effects of β , Ca , α , and Re are all taken into consideration. Furthermore, the perturbative weakly nonlinear approach we utilize also serves as a complementary theoretical tool to fully nonlinear numerical techniques, allowing the exploration of a range of key morphological pattern-forming behaviors in a simpler, less expensive fashion. In seeking to bolster the pragmatic and scholarly relevance of our study, in the rest of this paper we ensure that the values of all relevant dimensionless parameters we use (β , Ca , α , and Re) are consistent with realistic physical quantities related to existing radial Hele-Shaw cell arrangements and material properties of the fluids [2,5–11,17,18,23].

III. PATTERN-FORMATION DYNAMICS IN THE WEAKLY NONLINEAR REGIME

In this section we utilize the mode-coupling equations (8)–(15) to examine how the viscosity and density ratios, as well as the capillary and the Reynolds numbers, affect the shape of radial fingering patterns at weakly nonlinear stages of the dynamics. It should be clear that we have no intention of precisely recreating the advance time, complex radial Hele-Shaw cell patterns obtained by experiments [17,18] and numerical simulations [19]. In fact, the central objective of our weakly nonlinear study is to extract useful physical information about the complicated, fully nonlinear pattern-forming dynamics of the system, already at the lowest nonlinear order (i.e., at second order in ζ). In addition, we do that by describing the relevant pattern-forming and finger proliferation mechanisms (e.g., finger widening, narrowing, splitting, sidebranching, finger quadrifurcation, etc.) by conveniently utilizing the interaction of just a few pertinent Fourier modes. In this manner, we intend to predict and capture the most prominent nonlinear behaviors that will eventually emerge at advanced time stages of the radial Hele-Shaw cell dynamics. This is examined both in the absence (Sec. III A) and in the presence (Sec. III B) of inertial effects.

To have access to the possible shapes of the fingering structures, we consider the nonlinear coupling of a finite number N of morphologically relevant Fourier modes and rewrite Eq. (8) in terms of the real-valued cosine amplitudes $a_n = \zeta_n + \zeta_{-n}$. The time evolution of such mode amplitudes can then be obtained by numerically solving the corresponding coupled nonlinear differential equations. Once this is done, the shape of the evolving interface can be easily acquired by using $\zeta(\theta, t) = \zeta_0 + \sum_{n=1}^N a_n(t) \cos n\theta$.

At the early nonlinear time regime it is known that finger-sharpening, -widening, and -splitting phenomena can be described by considering the influence of a fundamental mode n on the growth of its harmonic $2n$. It has been shown [30] that an enhanced tendency of the outward moving fingers of the inner fluid to get wider (narrower) occurs when $a_{2n} < 0$ ($a_{2n} > 0$). So a negative (positive) growth for the cosine amplitude of the first-harmonic mode $2n$ would mean a tendency toward finger widening (sharpening) of the displacing fluid.

Moreover, as proposed in Refs. [31,32], if the harmonic cosine mode amplitude a_{3n} is positive and sufficiently large, it can produce interfacial lobes branching out sideward, leading to threefold sidebranching fingering patterns similar to those structures normally formed during crystal growth processes [33,34]. Likewise, we can associate the growth of the mode amplitude a_{4n} with the formation of four interfacial lobes at the fingertips of the displacing fluid, characterizing a quadrifurcation phenomenon. Similar descriptions would apply to higher Fourier modes.

It should be noted that, in real experiments, the occurrence of such quadrifurcation (or higher-order) fingering events is not commonly observed. In general, the prevalent detected experimental behavior is the emergence of fingertip-splitting (or finger bifurcation) phenomena. However, at higher capillary number values, more complex ramified structures may arise that do not necessarily come from successive bifurcations [11,35]. It is also worth noting that finger quadrifurcation is indeed revealed by numerical simulations performed in the high-capillary-number regime [see, for instance, Figs. 11(b) and 14(b) in Ref. [19]]. On the basis of these simple mode-coupling fingering mechanisms, in the following we consider the nonlinear coupling of the representative modes n , $2n$, $3n$, and $4n$ and analyze how the controlling parameters of our system (β , Ca , α , and Re) impact the time evolution and the shapes of the interfacial patterns in radial Hele-Shaw flows.

A. Effects of β and Ca in the absence of inertia

We begin our discussion by analyzing Fig. 2, which focuses on the noninertial limit ($\text{Re} = 0$) of our theoretical model. In the top panels of Fig. 2, we depict the fluid-fluid interface time evolution by considering the interaction of four representative cosine modes ($n = 5$, $2n = 10$, $3n = 15$, and $4n = 20$). The choice of $n = 5$ as the fundamental mode is made without loss of generality: It turns out that $n = 5$ is an unstable mode at $t = 0$ [$\dot{\zeta}_5(0) > 0$]. If one chooses another unstable Fourier mode as being the fundamental mode at $t = 0$, the basic physical results are similar to the ones obtained for $n = 5$. In the bottom panels, we plot the corresponding evolution of the rescaled cosine amplitudes $a_n(t)/R(t)$ for each of these Fourier modes. The interfaces are plotted in the absence of inertia, for $\beta = 5$, and for different values of the capillary number Ca : (a) 800, (b) 4000, and (c) 8000. It should be noted that if other relatively small values of β (for example, $\beta = 2.5$, 7.5 , or 10) are used in Fig. 2, equivalent behaviors for the interface dynamics would be obtained. This remark is also valid with respect to Fig. 5. All patterns illustrated in Fig. 2 have the same initial amplitudes $a_n(0) = 5 \times 10^{-2}$ and $a_{2n}(0) = a_{3n}(0) = a_{4n}(0) = 0$. In this way, we can ensure that the initial growth of the modes $2n$, $3n$, and $4n$ are driven solely by nonlinear effects. In other words, by applying such initial conditions we guarantee that the phenomena of finger splitting, sidebranching, and quadrifurcation are spontaneously induced by the weakly nonlinear terms of Eq. (8). In Fig. 2 the patterns evolve during the time interval $0 \leq t \leq t_f$, where t_f is the time at which successive interfaces are about to cross one another. This criterion for determining t_f is justified by the fact that the crossing of the interfaces (i.e., the occurrence of backward interface motion) is detected neither in experiments [5–11,17,18] nor in fully nonlinear simulations [12–14,19] of radial Hele-Shaw flows. Therefore, we adopt $t = t_f$ as the upper bound time for the validity of our theoretical approach.

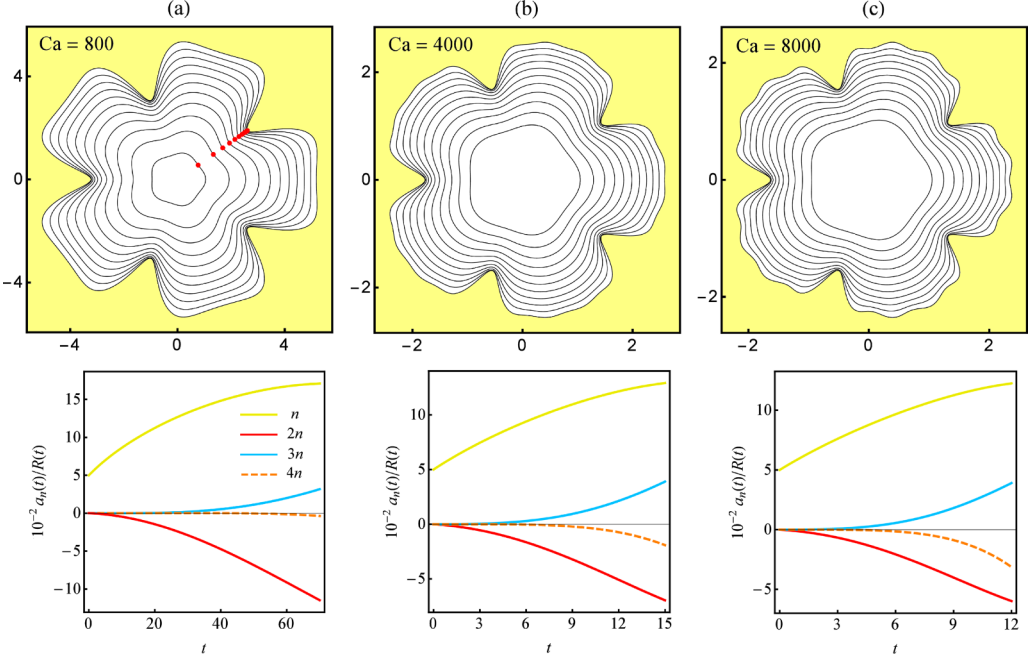


FIG. 2. Snapshot of the weakly nonlinear fluid-fluid interface (top panels), illustrating typical fingering patterns during radial Hele-Shaw flows, in the absence of inertial effects ($Re = 0$). The corresponding time evolution of the rescaled cosine amplitudes $a_n(t)/R(t)$ for modes n , $2n$, $3n$, and $4n$, where $n = 5$, is depicted in the bottom panels. The values taken for the capillary number are (a) $Ca = 800$, (b) $Ca = 4000$, and (c) $Ca = 8000$. In addition, we set $\beta = 5$ and the final times used are (a) $t_f = 70$, (b) $t_f = 15$, and (c) $t_f = 12$. The small dots shown in Fig. 2(a) display the time evolution of the base of a finger (fjord), located at an angle $\theta = \pi/5$.

By examining Fig. 2(a), we observe a nearly circular initial interface evolving to a five-fingered structure determined by the growth of the fundamental mode $n = 5$. Then, as time advances, the fingertips get increasingly wider and the onset of the classical fingertip-splitting phenomenon can be identified. Recall that finger-splitting morphology is generated by the negative growth of the first-harmonic mode $2n$ ($a_{2n} < 0$). We do verify this behavior in the bottom panel of Fig. 2(a), where a_{2n} dominates the dynamics over the other harmonic modes ($3n$ and $4n$) and evolves assuming negative values.

We continue by analyzing what happens to the interfacial patterns when higher values of capillary number are considered. Thus, in Figs. 2(b) and 2(c), we set $Ca = 4000$ and 8000 , respectively. Notice that in the pattern shown in Fig. 2(b) for $Ca = 4000$, the conventional splitting phenomenon (plain tip bifurcation) gives place to a more complex structure, characterized by the occurrence of a mild quadrifurcation of the fingertips. By inspecting the bottom row of Fig. 2, we can associate this behavior with the fact that the evolution of the mode $4n$ starts to increase negatively, whereas the growth of the amplitude a_{2n} becomes less intense. Then, if we keep increasing the capillary number to 8000 [Fig. 2(c)], we verify an enhanced growth of the mode $4n$ and a larger decrease of the magnitude of a_{2n} , yielding to an evident finger quadrifurcation event. It is worthwhile to note that even though the amplitude of mode $3n$ increases for higher capillary numbers, this is not enough to provoke the emergence of sidebranching formation (i.e., a finger trifurcation phenomenon) in the resulting finger morphology. These weakly nonlinear findings, which reveal a favored finger proliferation behavior as Ca is increased, are in line with the fully nonlinear numerical results recently obtained in Ref. [19]. It is reassuring to be able to assess important aspects of their fully nonlinear numerical study (which, by the way, neglects inertial effects) via a simpler weakly nonlinear theoretical approach.

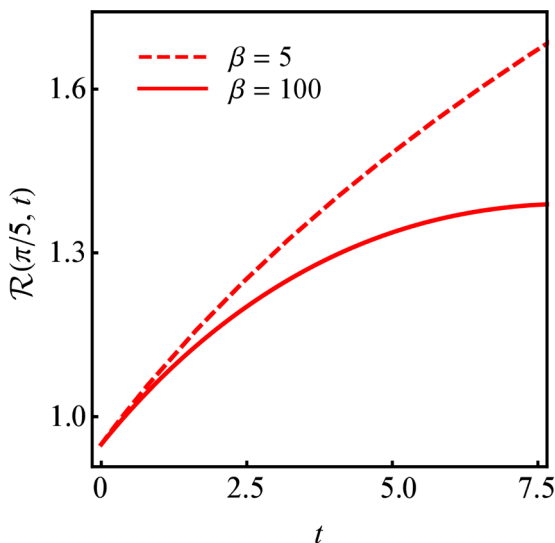


FIG. 3. Variation of the finger base position $\mathcal{R}(\pi/5, t)$ with time t for two values of the viscosity ratio: $\beta = 5$ (dashed curve) and $\beta = 100$ (solid curve). The remaining physical parameters and initial conditions considered in this figure are the same as those used in Fig. 2(a).

As mentioned in Sec. I, for large viscosity ratios β , both advance-time experiments [17,18] and fully nonlinear simulations [19] have found that the points located at the base of the fingers (fjords) simply do not move, defining the so-called stagnation points. Nonetheless, these fully nonlinear studies have also verified that the finger base positions do move away from the injection point during the pattern-formation process when lower values of β are considered. Therefore, no stagnation points are observed for such lower values of β in Refs. [17–19]. Here we investigate if this interesting nonstagnant finger base behavior can be caught at weakly nonlinear stages of the dynamics. This is done in the top panel of Fig. 2(a), where the small dots represent the time evolution of the finger base positions for a small value of the viscosity ratio ($\beta = 5$), an angle $\theta = \pi/5$, and $\text{Ca} = 800$. Notice that, in Fig. 2(a), we observe an evident reduction in the velocity of the small dots as time advances. Despite this deceleration, we can also see that the finger base position keeps moving outward during the injection process. This behavior characterizes the absence of the mentioned stagnation points at the onset of the nonlinear effects for $\beta = 5$. Similar conclusions can be reached for higher values of the capillary number [see Figs. 2(b) and 2(c)].

Complementary information about this issue is provided by Fig. 3, which depicts the time evolution of the finger base positions $\mathcal{R}(\pi/5, t)$ for two viscosity ratios: a small one ($\beta = 5$, dashed curve) and a large one ($\beta = 100$, solid curve). By inspecting Fig. 3, we observe that for $\beta = 5$, the base of the fingers keeps moving away from the injection point as time progresses. In fact, one can see that the dashed curve shows no tendency to saturation, still presenting a positive slope even for the largest time considered. In contrast, when a large value of viscosity ratio is used ($\beta = 100$), the finger base evolution slows down as time advances such that the solid curve tends to saturate its growth and eventually reaches a stagnation point position. These weakly nonlinear findings are in accord with the fully nonlinear results presented in Refs. [17–19].

Unfortunately, the experimental studies performed in Refs. [17,18] do not provide specific quantitative information about the time evolution of the base of the fingers as the viscosity ratio β is changed. Rather, they explore global dynamical issues related to the modification of the overall patterns' morphologies for varying viscosity ratios at later times, when the fingers are fully developed. For this reason we cannot directly compare our weakly nonlinear theoretical findings more quantitatively to the fully nonlinear experimental data reported in Refs. [17,18]. Nonetheless, by

inspecting the experimental patterns displayed in Refs. [17,18] (for instance, Fig. 2 in [17] and Fig. 1 in [18]), one clearly verifies that the fingering patterns show the presence of an inner circular region of complete displacement of the outer fluid. It is also apparent that such an inner circle increases with decreasing viscosity ratio β . Despite the current impossibility of a more quantitative comparison between theory and experiments, the experimental findings of Refs. [17,18] are consistent with the theoretical results obtained analytically in this work and numerically in Ref. [19]: At low viscosity ratios, the whole circular region expands (including the base of the fingers), resulting in the detected nonstagnant behavior.

The physical origin of the nonstagnant behavior of the finger bases at low viscosity ratio can be understood by the notion of the fluid mobility $M_j = b^2/12\eta_j$. At low viscosity ratio $\beta = \eta_2/\eta_1$, the mobility of fluid 2 is increased, meaning that it can be more easily swept by fluid 1, making the base of the finger advance more easily as time progresses. An additional reason for such a nonstagnant behavior has been presented in Ref. [19]: At low viscosity ratio the curvature of the finger base is relatively low, decreasing surface tension effects and thus favoring finger base motion.

B. Inertia-induced effects: Combined role of β , Ca, α , and Re

In this section we concentrate our attention on understanding the role played by inertial effects on the development of radial fingering in Hele-Shaw cells, under a quite general physical situation involving arbitrary viscosity and density ratios, for a range of allowed values of the capillary number. We stress that, with the consideration of inertia, in addition to parameters β and Ca considered in Sec. III A, one must keep in mind the action of the parameters α and Re.

For the sake of clarity and in the interest of better comprehending the effects of the various physical parameters, instead of immediately addressing weakly nonlinear issues, we initiate our discussion by briefly analyzing some important purely linear aspects of the system. Figure 4 plots the linear growth rate $\lambda(n) = \zeta_n/\zeta_n$ as a function of mode n , at time $t = 70$, for two cases where (i) inertial effects are neglected (Re = 0, dashed curve) and (ii) inertia is relevant (Re = 0.1, solid curves). Here we set $\beta = 5$ and Ca = 1000 and consider different values of the density ratio α . First, we verify that, in the realm of a linear theory, inertia tends to stabilize the viscous fingering instability (solid curves located below the dashed one). Moreover, it is evident that this stabilizing

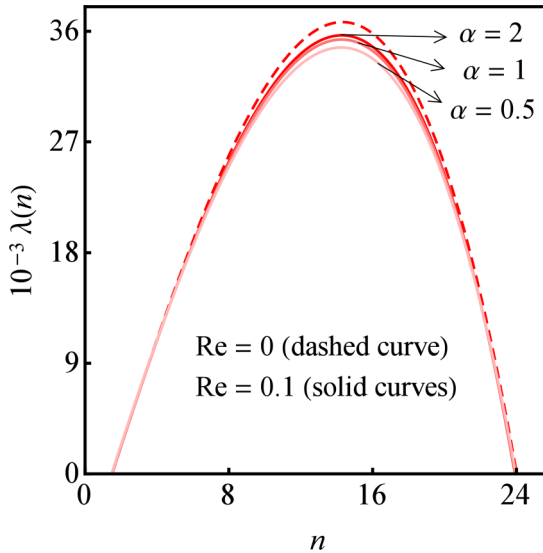


FIG. 4. Linear growth rate as a function of the Fourier mode n , for Re = 0 (dashed curve) and Re = 0.1 (solid curves), for three different values of α : 2, 1, and 0.5. Here $\beta = 5$ and Ca = 1000.

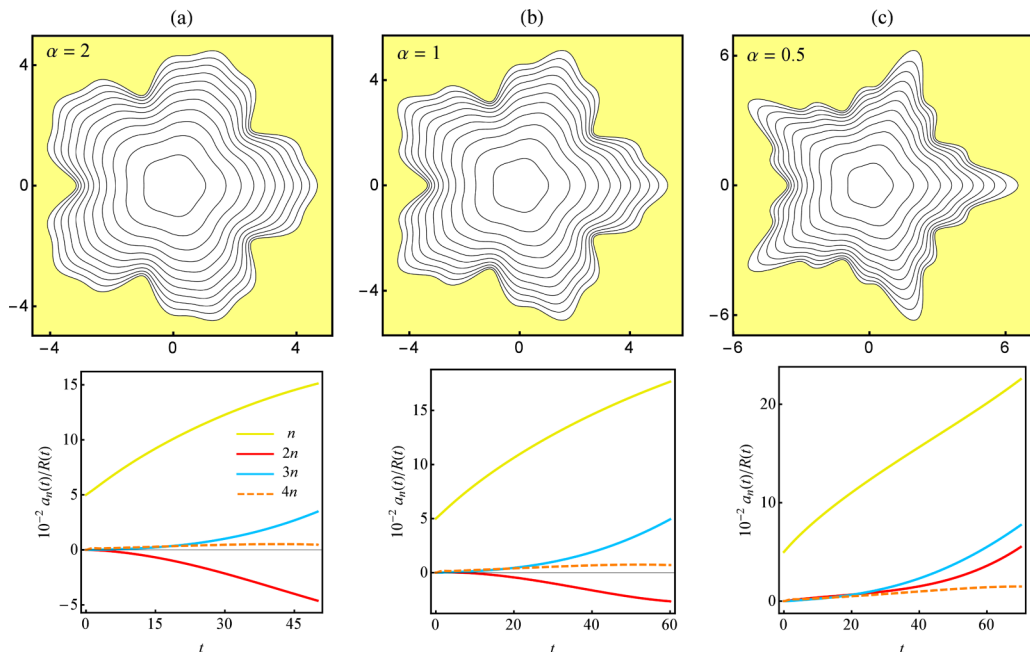


FIG. 5. Snapshot of the weakly nonlinear time evolution of the fluid-fluid interface (top panels) when inertial effects are of relevance ($Re = 0.1$). The corresponding evolution of the rescaled cosine amplitudes $a_n(t)/R(t)$ for modes n , $2n$, $3n$, and $4n$, where $n = 5$, is depicted in the bottom panels. The values taken for the density ratio are (a) $\alpha = 2$, (b) $\alpha = 1$, and (c) $\alpha = 0.5$. Additionally, we set $\beta = 5$ and $Ca = 1000$. The final times are (a) $t_f = 50$, (b) $t_f = 60$, and (c) $t_f = 70$.

effect is stronger for lower values of the density ratio α . Physically, this means that the higher the density of the displacing fluid, the weaker the Saffman-Taylor instability.

Another interesting and useful linear concept is the critical mode n_c , obtained by setting $\lambda(n)|_{n=n_c} = 0$. It defines the width of the band of unstable modes. From Fig. 4 it is clear that n_c does not change when inertial effects are taken into account. A similar conclusion is valid for the fastest growing mode n_{\max} [acquired by setting $d\lambda(n)/dn|_{n=n_{\max}} = 0$]. Consequently, at the purely linear level, one can say that the number of emerging fingers (predicted by the closest integer to n_{\max}) should not be influenced by the action of inertia. Other than these issues, not much can be extracted from Fig. 4 regarding the specific shapes of the resulting fingering patterns, when inertia is significant. All these linear findings may give the impression that inertia would not have a dramatic impact in determining the shape of the fingering structures. However, as we will see below, this is not at all the case.

In order to assess key information about the morphology of the arising patterns under the presence of inertia, we must turn to the weakly nonlinear dynamics. This is done in Fig. 5, which illustrates the weakly nonlinear patterns that arise when inertial effects are taken into consideration. In the top panels we plot the shape of the fluid-fluid interface for $Re = 0.1$, $\beta = 5$, and three decreasing values of density ratio α : (a) 2, (b) 1, and (c) 0.5. Here we take $Ca = 1000$. Similar to Fig. 2, in the bottom panels of Fig. 5 we depict the time evolution of the rescaled cosine amplitudes $a_n(t)/R(t)$ for four Fourier modes n , $2n$, $3n$, and $4n$, where we set the fundamental mode as $n = 5$. The initial conditions are $a_n(0) = 5 \times 10^{-2}$ and $a_{2n}(0) = a_{3n}(0) = a_{4n}(0) = 0$. In addition, we take $\dot{a}_n(0) = 1.1 \times 10^{-2}$ and $\dot{a}_{2n}(0) = \dot{a}_{3n}(0) = \dot{a}_{4n}(0) = 0$.

It is quite apparent that the patterns shown in Fig. 5 for $Re \neq 0$ are very different from the ones illustrated in Fig. 2 for which $Re = 0$. For instance, in contrast to what is shown Fig. 2, in Fig. 5

we do not observe the occurrence of either fingertip splitting or finger quadrifurcation. Instead, regardless the value of α , the most prevalent morphological phenomenon is indeed sidebranching or the appearance of finger trifurcation. Thus, when inertial effects are relevant, the traditional tip-split and quadrifurcated fingers are replaced by threefold fingering structures. This interesting change in the morphology of the patterns can be understood by analyzing the bottom row of Fig. 5, where we verify an inhibition in the growth of mode $4n$, accompanied by an increase in the growth of mode $3n$. Recall that a positive sign for a_{3n} favors sidebranching formation [31,32]. Moreover, it can also be noted in Fig. 5(a) that the amplitude of a_{2n} remains negative all the time, favoring the formation of wide fingers. As a result, in Fig. 5(a) we observe fingers that are relatively wide but that branch out sideways.

Nevertheless, a different behavior is unveiled when we decrease the value of the density ratio α , i.e., when we consider an inner fluid with an equal or lower density. In particular, notice that for the density-matched case $\alpha = 1$ [Fig. 5(b)], the final interfacial pattern presents fingers that still branch out sideways but are a bit less wide than the corresponding finger for the pattern illustrated in Fig. 5(a). Within our mode-coupling scheme, this can be justified by the increase of the growth of the mode amplitude a_{3n} together with a less prominent growth observed for the mode $2n$ (which, incidentally, became less negative). If we keep decreasing α until the inner fluid has a lower density than the outer fluid [for instance, for $\alpha = 0.5$, as in Fig. 5(c)], we observe a change in the sign of the mode amplitude for $2n$, so a_{2n} becomes positive. Remember that this is precisely the sign of a_{2n} that favors the formation of narrow fingers [30]. As a consequence, we still have the formation of three-lobed sidebranching shapes, but now presenting long and narrow fingertips. Finally, it is also worth noting that, as opposed to what occurred in Fig. 2, finger quadrifurcation is not detected in Fig. 5. This can be explained by the fact that the mode amplitude a_{4n} just changes modestly as time proceeds in the bottom panels of Figs. 5(a)–5(c).

This predominance of sidebranching behavior when inertia is taken into account in injection-driven radial Hele-Shaw flows has also been recently found to occur in lifting (time-dependent gap) Hele-Shaw cell displacements [29]. As a matter of fact, we note that inertia could be a possible physical cause leading to the development of patterns presenting simple three-lobed fingers (see, for instance, Fig. 1 in Ref. [5]) or even complex sidebranching, fractal structures [see, for example, Fig. 16(b) in Ref. [35]], in some injection-driven radial Hele-Shaw flows.

At this point, we examine the tendency towards finger base stagnation or activeness under the presence of inertial effects. To do that, in Fig. 6 we illustrate the time evolution of the base of the fingers when inertia acts, by setting $Re = 0.1$. This is similar to what we did in Fig. 3 for the zero-Reynolds-number situation. We use the same values of the viscosity ratios utilized in Fig. 3: $\beta = 5$ (dashed curves) and $\beta = 100$ (solid curves). For each value of β , we take $\alpha = 2, 1$, and 0.5 . The rest of the physical parameters and initial conditions used in Fig. 6 are the same as those utilized in Fig. 5. By inspecting Fig. 6, first we notice that the three dashed curves, which correspond to different values of α , overlap each other. This means that inertia has no influence on the stagnation point behavior when low values of the viscosity ratio are considered. On the other hand, from Fig. 6 we verify that for a larger viscosity ratio ($\beta = 100$) the evolution of the finger bases changes for different values of the density ratio α . One can check this by noticing that the overlapping curves for $\beta = 5$ present a nonzero slope at the final time computed. Consequently, when $\beta = 5$ the finger bases do not reach a stationary state and keep moving away from the injection point. In contrast, when we increase the value of the viscosity ratio ($\beta = 100$) and consider larger values of α , we observe a slowing down in the dynamics of the finger base positions. This is clearly verified in Fig. 6, where the darker solid curve for $\alpha = 2$ tends to saturate as time increases, eventually leading to a stagnation point presenting a vanishing interfacial velocity.

Recall that the analysis of Fig. 5 revealed that when we consider lower values of the density ratio α and a fixed Ca , a change in the morphology of the interfacial patterns is observed: Broader fingers are replaced by narrower ones. This is induced by the change in the sign of the first-harmonic amplitude a_{2n} . With this fact in mind, we close this section by examining Fig. 7, which presents a morphological phase diagram for the emerging patterns in the parameter space (Ca, α) . The representative interfacial

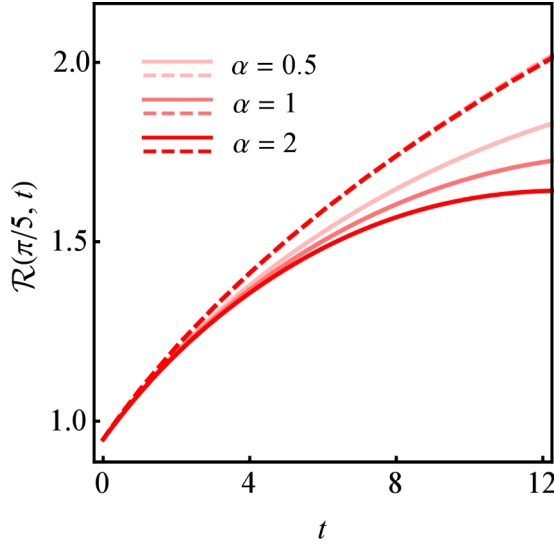


FIG. 6. Plot of the finger base position $\mathcal{R}(\pi/5, t)$ as a function of time t for two values of the viscosity ratio: $\beta = 5$ (dashed curve) and $\beta = 100$ (solid curves). Three values of the density ratio are considered: $\alpha = 2$, 1, and 0.5. Note that in the dashed curve associated with $\beta = 5$ and $\alpha = 2$ there are in fact three overlapping curves (two indistinguishable dashed curves for $\alpha = 1$ and $\alpha = 0.5$ lie hidden). Here we set $\text{Re} = 0.1$ and $\text{Ca} = 1000$.

patterns shown in Fig. 7 are plotted for $\beta = 5$, $\text{Re} = 0.1$, and the same initial perturbation amplitudes used in Fig. 5. In such a diagram we can identify the establishment of two different morphological regions, separated by a dashed line: The first region (located below the dashed line) is characterized by the occurrence of sidebranching patterns exhibiting an elongated, notably sharp, central finger

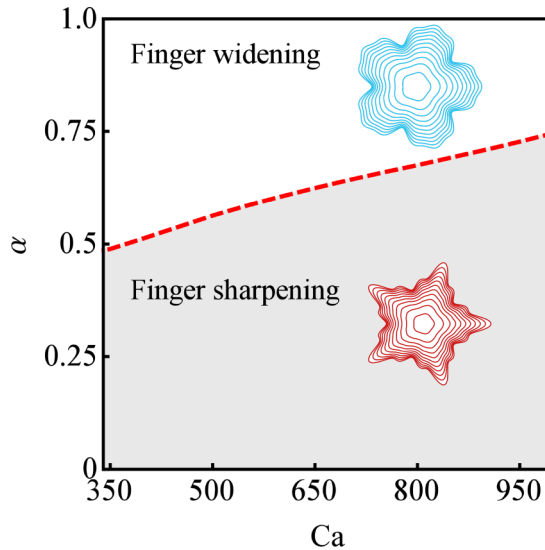


FIG. 7. Morphological phase diagram in the parameter space (Ca, α) . The dashed line delimits the boundary between the two different morphological regions. The development of sidebranching patterns is observed in both regions, where either finger widening or finger sharpening may occur. Here we take $\beta = 5$ and $\text{Re} = 0.1$.

(which occurs for $a_{2n} > 0$), whereas the region located above the dashed line is typified by the appearance of a different type of sidebranching shapes, stubbier structures, having shorter central fingers presenting wider tips (which arise for $a_{2n} < 0$). The dashed line separating the regions in Fig. 7 is obtained by evaluating the range of values for the parameters Ca and α such that the first-harmonic amplitude is equal to zero [$a_{2n}(t_f) = 0$] for the final time $t_f = 70$. Interestingly enough, as opposed to the situations without inertia discussed in Sec. III A, where various interfacial profiles may proliferate (via finger bifurcation, quadrifurcation, etc.), when inertia is present, only threefold sidebranching structures are detected while Ca and α sweep across a range of values.

The detection of the sidebranching trifurcated structures (two side lobes accompanied by a central protuberance) that form at finite Reynolds numbers is somewhat surprising. Such a three-lobed finger configuration resembles the dendritic sidebranching shapes that are normally encountered in anisotropic crystal growth processes [33,34]. Similar types of sidebranching fingering morphologies are also found during injection-driven radial flows involving intrinsically anisotropic fluids (e.g., shear-thinning or yield stress fluids) in Hele-Shaw cells [32,36,37] as well as in situations where anisotropy is imposed by the growth environment (for instance, in Hele-Shaw cells presenting etched plates [8,38]). However, in our current study there is no apparent anisotropy present and still sidebranching structures emerge at finite Reynolds numbers. This is quite intriguing. Although our weakly nonlinear approach does reveal an enhanced growth of mode $3n$ for sizable Re , lamentably, at this point, we do not have a good physical explanation for this fact. Therefore, the understanding of the physical mechanism leading to sidebranching formation in our system remains an open question.

IV. CONCLUSION

The overwhelming majority of the pattern-forming investigations of the radial viscous fingering instability focus on the limits of very large or infinite viscosity ratios. However, recent experiments [17,18] and numerical simulations [19] demonstrate that the advance time fully nonlinear shapes of the patterns change dramatically when the viscosity ratio is varied. It has been found that viscous and capillary effects control the ultimate profile shapes, where the number of lobes at the fingertips tends to increase with the capillary number. Moreover, it has also been revealed that the base of the fingers does not stagnate under finite-viscosity-ratio conditions. Despite the importance of these fully nonlinear findings, these studies do neglect the effects of inertia on the pattern-formation process.

In this work we analyzed the development of viscous fingering patterns in radial Hele-Shaw cells for a general situation in which the effects of inertia, capillarity, viscosity, and density ratios are all taken into account. Specifically, we made use of a relatively simple analytical mode-coupling theory to try to understand how these important physical effects impact the morphology of weakly nonlinear fingering patterns. The main differentiating factor of our model from the vast literature of Hele-Shaw cell modeling is its ability to capture (in the absence of inertia) and predict (in the presence of inertia) the most prominent nonlinear pattern-forming behaviors via a relatively simple, less expensive theoretical description (in comparison with usual numerical models) of this emblematic fluid dynamic problem [17–19].

If inertial effects are neglected, we have found that the shape of the weakly nonlinear fingering structures has a strong dependence on the viscosity ratio and capillary number. In particular, we showed that fingers proliferate (through finger-bifurcation and finger-quadrifurcation mechanisms) when the capillary number is increased. Furthermore, we have verified that suppression of finger base stagnation can be detected already at weakly nonlinear time stages of the flow. These weakly nonlinear results in the absence of inertia are consistent with existing experimental and numerical studies of the problem.

On the other hand, when inertia is taken into account, we have verified that two other controlling parameters come into play, namely, the density ratio and the Reynolds number (which controls the action of inertia). Under the circumstances in which inertia is non-negligible, we observed that the resulting pattern-forming structures are very different from their noninertial counterparts. In fact,

we have detected the formation of threefold sidebranched patterns for which finger-widening and -sharpening behaviors are regulated by the density ratio and the capillary number. In closing, it should be noted that these nonlinear inertia-mediated predictions still need to be checked by advance-time numerical simulations and experiments.

ACKNOWLEDGMENTS

J.A.M. thanks CNPq (Brazilian Research Council) for financial support under Grant No. 304821/2015-2. E.O.D. acknowledges financial support from FACEPE through PPP Project No. APQ-0800-1.05/14.

-
- [1] P. G. Saffman and G. I. Taylor, The penetration of a fluid into a porous medium or Hele-Shaw cell containing a more viscous liquid, *Proc. R. Soc. London Ser. A* **245**, 312 (1958).
 - [2] G. M. Homsy, Viscous fingering in porous media, *Annu. Rev. Fluid Mech.* **19**, 271 (1987); K. V. McCloud and J. V. Maher, Experimental perturbations to Saffman-Taylor flow, *Phys. Rep.* **260**, 139 (1995); J. Casademunt, Viscous fingering as a paradigm of interfacial pattern formation: Recent results and new challenges, *Chaos* **14**, 809 (2004).
 - [3] J. Bataille, Stabilité d'un écoulement radial non miscible, *Rev. Inst. Fr. Pet. Ann. Combust. Liq.* **23**, 1349 (1968).
 - [4] S. D. R. Wilson, A note on the measurement of dynamic contact angles, *J. Colloid Interface Sci.* **51**, 532 (1975).
 - [5] L. Paterson, Radial fingering in a Hele-Shaw cell, *J. Fluid Mech.* **113**, 513 (1981).
 - [6] S. N. Rauseo, P. D. Barnes, and J. V. Maher, Development of radial fingering patterns, *Phys. Rev. A* **35**, 1245 (1987).
 - [7] S. E. May and J. V. Maher, Fractal dimension of radial fingering patterns, *Phys. Rev. A* **40**, 1723 (1989).
 - [8] J. D. Chen, Radial viscous fingering patterns in Hele-Shaw cells, *Exp. Fluids* **5**, 363 (1987).
 - [9] J. D. Chen, Growth of radial viscous fingers in a Hele-Shaw cell, *J. Fluid Mech.* **201**, 223 (1989).
 - [10] H. Thomé, M. Rabaud, V. Hakim, and Y. Couder, The Saffman-Taylor instability: From the linear to the circular geometry, *Phys. Fluids A* **1**, 224 (1989).
 - [11] O. Praud and H. L. Swinney, Fractal dimension and unscreened angles measured for radial viscous fingering, *Phys. Rev. E* **72**, 011406 (2005).
 - [12] P. Fast and M. J. Shelley, Moore's law and the Saffman-Taylor instability, *J. Comput. Phys.* **212**, 1 (2006).
 - [13] J. Mathiesen, I. Procaccia, H. L. Swinney, and M. Thrasher, The universality class of diffusion-limited aggregation and viscous fingering, *Europhys. Lett.* **76**, 257 (2006).
 - [14] S. W. Li, J. S. Lowengrub, J. Fontana, and P. Palfy-Muhoray, Control of Viscous Fingering Patterns in a Radial Hele-Shaw Cell, *Phys. Rev. Lett.* **102**, 174501 (2009).
 - [15] S. B. Gorell and G. M. Homsy, A theory of the optimal policy of oil recovery by secondary displacement processes, *SIAM J. Appl. Math.* **43**, 79 (1983); J. P. Stokes, D. A. Weitz, J. P. Gollub, A. Dougherty, M. O. Robbins, P. M. Chaikin, and H. M. Lindsay, Interfacial Stability of Immiscible Displacement in a Porous Medium, *Phys. Rev. Lett.* **57**, 1718 (1986).
 - [16] F. Fayers, *Enhanced Oil Recovery* (Elsevier, Amsterdam, 1981).
 - [17] D. Perugini and G. Poli, Viscous fingering during replenishment of felsic magma chambers by continuous inputs of mafic magmas: Field evidence and fluid-mechanics experiments, *Geology* **33**, 5 (2005).
 - [18] I. Bischofberger, R. Ramachandran, and S. R. Nagel, An island of stability in a sea of fingers: Emergent global features of the viscous-flow instability, *Soft Matter* **11**, 7428 (2015).
 - [19] S. J. Jackson, D. Stevens, H. Power, and D. Giddings, A boundary element method for the solution of finite mobility ratio immiscible displacement in a Hele-Shaw cell, *Int. J. Numer. Methods Fluids* **78**, 521 (2015).

- [20] P. Gondret and M. Rabaud, Shear instability of two-fluid parallel flow in a Hele-Shaw cell, *Phys. Fluids* **9**, 3267 (1997).
- [21] C. Ruyer-Quil, Inertial corrections to the Darcy law in a Hele-Shaw cell, *C. R. Acad. Sci. II B* **329**, 337 (2001).
- [22] F. Plouraboue and E. J. Hinch, Kelvin-Helmholtz instability in a Hele-Shaw cell, *Phys. Fluids* **14**, 922 (2002).
- [23] C. Chevalier, M. Ben Amar, D. Bonn, and A. Lindner, Inertial effects on Saffman-Taylor viscous fingering, *J. Fluid Mech.* **552**, 83 (2006).
- [24] A. He and A. Belmonte, Inertial effects on viscous fingering in the complex plane, *J. Fluid Mech.* **668**, 436 (2011).
- [25] E. O. Dias and J. A. Miranda, Inertial effects on rotating Hele-Shaw flows, *Phys. Rev. E* **83**, 046311 (2011).
- [26] E. O. Dias and J. A. Miranda, Influence of inertia on viscous fingering patterns: Rectangular and radial flows, *Phys. Rev. E* **83**, 066312 (2011).
- [27] Q. Yuan and J. Azaiez, Inertial effects of miscible viscous fingering in a Hele-Shaw cell, *Fluid Dyn. Res.* **47**, 015506 (2015).
- [28] Q. Yuan and J. Azaiez, Inertial effects in cyclic time-dependent displacement flows in homogeneous porous media, *Can. J. Chem. Eng.* **93**, 1490 (2015).
- [29] P. H. A. Anjos, E. O. Dias, and J. A. Miranda, Inertia-induced dendriticlike patterns in lifting Hele-Shaw flows, *Phys. Rev. Fluids* **2**, 014003 (2017).
- [30] J. A. Miranda and M. Widom, Radial fingering in a Hele-Shaw cell: A weakly nonlinear analysis, *Physica D* **120**, 315 (1998).
- [31] M. Constantin, M. Widom, and J. A. Miranda, Mode-coupling approach to non-Newtonian Hele-Shaw flow, *Phys. Rev. E* **67**, 026313 (2003).
- [32] J. V. Fontana, S. A. Lira, and J. A. Miranda, Radial viscous fingering in yield stress fluids: Onset of pattern formation, *Phys. Rev. E* **87**, 013016 (2013).
- [33] L. N. Brush, R. F. Sekerka, and G. B. McFadden, A numerical and analytical study of nonlinear bifurcations associated with the morphological stability of two-dimensional single crystals, *J. Cryst. Growth* **100**, 89 (1990).
- [34] P. P. Debroy and R. F. Sekerka, Weakly nonlinear morphological instability of a cylindrical crystal growing from a pure undercooled melt, *Phys. Rev. E* **53**, 6244 (1996).
- [35] Y. Couder, in *Perspectives in Fluid Dynamics—A Collective Introduction to Current Research*, edited by G. K. Batchelor, H. K. Moffatt, and M. G. Worster (Cambridge University Press, Cambridge, 2000), pp. 53–104.
- [36] L. Kondic, M. J. Shelley, and P. Palffy-Muhoray, Non-Newtonian Hele-Shaw Flow, and the Saffman-Taylor Instability, *Phys. Rev. Lett.* **80**, 1433 (1998).
- [37] P. Fast, L. Kondic, M. J. Shelley, and P. Palffy-Muhoray, Pattern formation in Non-Newtonian Hele-Shaw flow, *Phys. Fluids* **13**, 1191 (2001).
- [38] E. Ben-Jacob, R. Godbey, N. D. Goldenfeld, J. Koplik, H. Levine, T. Mueller, and L. M. Sander, Experimental Demonstration of the Role of Anisotropy in Interfacial Pattern Formation, *Phys. Rev. Lett.* **55**, 1315 (1985).